This is a repository copy of *Investigation of particle radiation and its effect on NO prediction in a pilot-scale facility for both air and oxy-coal combustion*.

White Rose Research Online URL for this paper:
http://eprints.whiterose.ac.uk/145024/

Version: Accepted Version

Investigation of particle radiation and its effect on NO prediction in a pilot-scale facility for both air and oxy-coal combustion

H. Huynh[a], A. G. Clements[b,*], J. Szuhánszki[b], W. F. Gale[a], L. Ma[b], D. B. Ingham[b], M. Pourkashanian[b]

[a]*Centre for Integrated Energy Research, School of Chemical and Process Engineering, Faculty of Engineering, University of Leeds, Leeds, LS2 9JT*
[b]*Energy 2050, Faculty of Engineering, University of Sheffield, Sheffield, S10 2TN*

Abstract

Radiation heat transfer plays an important role in pulverised coal combustion, influencing the overall combustion efficiency, pollutant formation and flame ignition and propagation. In this paper, the radiation properties of the particles as well as gas property models on the overall influence of the prediction of the formation of NO_x pollutants in a pulverised coal combustion have been investigated. The non-grey weighted sum of grey gases (WSGG) model has been employed to calculate the radiation of the gas phase coupled with the radiation interaction from the particulate phase. The Mie theory, as well as constant or linear models, have been employed to describe the particle radiative properties. The prediction results, calculated from the data from a 250 kW pilot scale combustion test facility (CTF), are compared against experimental measurements under air-fired condition and a range of oxyfuel conditions. The results show that the choice of radiation solution can have a considerable impact on the radiative heat transfer results, in which the Mie theory shows a significant improvement in the incident wall heat flux

*Corresponding author
Email address: `a.g.clements@sheffield.ac.uk` (A. G. Clements)

compared to the constant or linear models. Also, the more accurate solution employed for radiation of gases and particles considerably improves the NO_x prediction in the flame region.

Keywords: Radiative heat transfer, oxyfuel, combustion

1. Introduction

Although the global consumption of coal has undergone slower growth in recent years, coal is still expected to remain 24% of primary energy consumption in 2035 [1]. With increasing regulations focused on environmental protection, coal combustion modelling has received special attention for its potential role in reducing the environmental impact of utilising coal combustion, such as retrofits of traditional power plants and new designs of coal fired power plants for oxyfuel combustion, one of the main technologies for CO_2 capture. Radiation heat transfer is important in pulverised coal combustion because of the high temperatures reached within combustion furnaces, as well as the presence of participating species such as CO_2/H_2O, and solid-phase coal, char and fly-ash particles [2, 3]. The characteristics of radiative heat transfer under oxyfuel combustion are different from those of air-fired combustion, due to the higher concentration of participating species and potentially higher temperatures at elevated oxygen concentrations. Accurate calculations, taking into account the impact of the variable combustion medium, is considered to be a priority for retrofitting an existing unit to oxyfuel while maintaining similar temperatures and heat transfer characteristics [4, 5]. The accuracy in radiative modelling of the combustion process has a large effect on the overall prediction of the combustion efficiency, pollutant

2

formation and flame ignition and propagation. Accurate radiation modelling needs to consider both gaseous phase and particulate participation in the radiative mechanism. With the dominance of the radiative heat transfer of the particles compared to that of the gases in pulverised coal combustion, more attention needs to be focused on the radiative properties of particles [5].

The global gas property model which has been a preferred selection for complex combustion modelling, mostly due to its low computational expense, is the weighted sum of grey gases (WSGG) model. The first WSGG model applied for non grey media was proposed by Hotel and Sarofim [6] for use with the zonal method, and it has been demonstrated by Modest [7] for application as an arbitrary solution method. A widely used set of fitted coefficients for the WSGG model for combustion gases, absorption coefficients and weighting factors, was proposed by Smith [8]. However, these values were obtained at specific mole fraction ratios of H_2O and CO_2, which limits the use of these coefficients under oxyfuel conditions. This limitation was improved by Yin [9] for a wider range of discrete ratios and by Johansson [10] for a variable and wide range of CO_2 and H_2O ratios that better presented the radiative properties of the gas products for both air and oxyfuel combustion. One of the most recent set of coefficients for the WSGG model was developed by Kangwanpongpan [11], which was evaluated using the HITEMP 2010 spectroscopic database [12] for a wide range of CO_2 and H_2O ratios, and was chosen in this paper to describe the properties of non-grey gases.

The presence of the particles in coal-fired combustion has a significant effect on the radiative heat transfer mechanism [13, 14]. The radiative prop-

3

erties of the particles are complicated to define and depend on the particle composition, size, and the wavelength of the incoming radiation, and vary during the particle's trajectory through the furnace. Therefore, the accounting of the properties of the particles, namely emissivity and scattering coefficients, are conventionally simplified to be constant values in most simulation studies [15, 16]. It is necessary to employ global models for the radiative properties of gas-phase species in coupled computational fluid dynamics (CFD) calculations, which discard spectral fidelity in order to solve the radiative intensity field for integral values. With this disregard of the spectral locations, it is necessary to couple the particulate radiative properties into the global radiation property models using grey particle values.

The emission of nitrogen oxides from combustion systems is a significant pollutant source that is threatening the global environment. Mechanisms of NO_x formation and destruction processes in combustion systems are very complicated [17]. As NO_x species are trace species within the domain, the formation of the pollutants does not significantly affect the fluid dynamics or heat transfer of the combustion process, and so can be calculated as a post-processing step. This means that the accuracy in the predictions of flame temperature, volatile release, char burnout and aerodynamics are prerequisites to the prediction of NO_x formation [18]. This study will determine the sensitivity of the NO_x prediction to the choice of the radiation models.

The grey radiative properties for the gas and particles has been widely used in CFD modelling of pulverised coal combustion under oxyfuel conditions. Applying non-grey WSGG models can be found in some studies for pilot-scale [19, 20] and for large-scale furnaces [21, 22]. However, in these

4

studies, radiative properties of particle are assumed as constants. The purpose of this paper is to investigate the radiative heat transfer in pulverised coal combustion, focusing on the particle radiation and how this affects NO_x predictions. The non-grey WSGG model [11] was employed to describe the radiation of the gas and the Mie theory was used to describe the particle radiative properties. The modelling results were compared against the experimental data from [23] and experimental measurements for in-flame NO concentrations, which were obtained under air-fired and oxy-fired conditions.
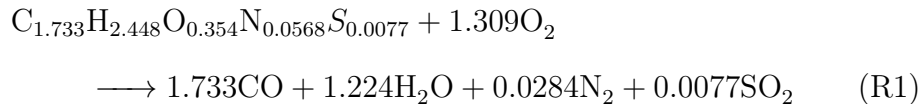
2. Numerical model

The commercial computational fluid dynamics (CFD) software ANSYS FLUENT v17.0 has been employed to simulate the PACT 250 kW air/oxy-fired CTF, which is part of the UKCCSRC PACT Core Facilities. The cylindrical furnace has an internal diameter of 0.9 m and is 4 m high. The furnace is lined with a 0.1 m thick refractory and the first 3 m are water cooled. The burner is a scaled version of a commercially available low-NO_x burner, which has been scaled to 250 kW_{th} and provided by Doosan Babcock. The primary stream and coal are supplied through a primary annulus and the secondary, tertiary annuli supply the majority of the swirled oxidiser. More details about the facility can be found in [24]. The properties of the coal investigated are shown in Table 1 and the operating conditions for both the air- and oxy-fired environments are listed in Table 2. The O_2 concentration in each case is also shown in Table 2, where the balance of gas composition is taken to be N_2 in the air case and CO_2 in the oxyfuel cases. Both cases were set up with a thermal load of 200 kW. User defined functions (UDFs) were used

to customise the radiative property models of the gas and particle phases. Three conditions have been considered, a baseline air-fired combustion case and two oxyfuel regimes, Oxy-27 (overall 27 vol.% O_2 and 73 vol.% CO_2 in the oxidiser) and Oxy-30 (overall 30 vol.% O_2 and 70 vol.% CO_2 in the oxidiser).

All of the cases presented in this study were calculated using a RANS approach, using the Reynolds stress model of Launder et al. [25] to model the unclosed terms. The Reynolds stress model has been found to produce better prediction results for the temperature and oxygen concentration in the recirculation zone [26] and better predictions of NO_x [27] than that when using the k-ε model. The particle size distribution is modelled using a Rosin Rammler distribution, where the mean particle diameter is 120 µm, and a spread parameter of 1.1. A total of forty particle diameters were used to describe the particle size distribution, resulting in 19,380 particle tracks for every 100 fluid iterations. Using more diameters did not change the solution.

The CTF was modelled using one quarter of the full geometry, exploiting the rotational symmetry of the furnace, resulting in a structured mesh containing about 1.4 million hexahedral cells. The heat flux through the furnace wall was modelled as a thin wall boundary condition, with the furnace wall thickness of 0.1 m having outer temperature of 350 K, and an internal emissivity of 0.8 [24]. The inlet and outlet surfaces were assumed to have an emissivity of 1. The single kinetic rate [28] was used to describe the devolatilisation of the coal particles, with the pre-exponential factor of 14,841 s^{-1} and an activation energy of 35.3 kJ/mol. A two-step global reaction mechanism was employed for the homogeneous combustion of an empirically

6

defined volatile species, reactions (R1) and (R2), and the eddy dissipation model was used for the turbulence-chemistry interaction:

$$C_{1.733}H_{2.448}O_{0.354}N_{0.0568}S_{0.0077} + 1.309O_2$$
$$\longrightarrow 1.733CO + 1.224H_2O + 0.0284N_2 + 0.0077SO_2 \qquad \text{(R1)}$$

$$CO + \frac{1}{2}O_2 \longrightarrow CO_2 \qquad \text{(R2)}$$

The surface char combustion reaction is described by the Smith intrinsic model [29], with kinetic parameters from [30]: a pre-exponential factor of 4×10^{-4} kg/(m^2.s.Pa) and an activation energy of 66 kJ/mol.

2.1. Radiative heat transfer

The radiative properties of the gas are described by the non-grey WSGG model, in which the total emissivity, ε, is the total weighted sum of grey gas emissivities, as

$$\varepsilon = \sum_{i=0}^{N_g} a_{g,i} \left(1 - e^{-\kappa_{g,i}s}\right) \qquad (1)$$

where N_g is the number of grey gases, $a_{g,i}$ and $\kappa_{g,i}$ are the emissivity weighting factor and absorption coefficient for the ith grey gas, respectively, s is the path length. The radiation transfer equation (RTE) for the ith grey gas through a medium of a mixture of the non-grey gases and the grey particles is expressed as follows:

7

$$\frac{\mathrm{d}I_i\left(\vec{r}, \vec{s}\right)}{\mathrm{d}s} = -\left(\kappa_{g,i}(\vec{r}) + \kappa_p(\vec{r}) + \sigma_p(\vec{r})\right) I_i\left(\vec{r}, \vec{s}\right) + a_{g,i}(\vec{r})\kappa_{g,i}(\vec{r})I_{b,g}\left(\vec{r}\right) \quad (2)$$
$$+ E_{p,i}\left(\vec{r}\right) + \frac{\sigma_p(\vec{r})}{4\pi} \int_{4\pi} I_i\left(\vec{r}, \vec{s}\,'\right) \Phi\left(\vec{s}.\vec{s}\,'\right) \mathrm{d}\Omega'$$

163   where $E_{p,i}(\vec{r})$ is the emission of the particles corresponding to the ith grey

164   gas at position $\vec{r}$, $I_i\left(\vec{r}, \vec{s}\right)$ is the radiative intensity at location $\vec{r}$ travelling in

165   direction $\vec{s}$, $I_{b,g}(\vec{r})$ is the black body intensity calculated at the temperature

166   at position $\vec{r}$, $\sigma_p(\vec{r})$ is the scattering coefficient of particles, $\Phi\left(\vec{s}.\vec{s}\,'\right)$ is the

167   scattering phase function and Ω' denotes solid angle. The non-grey WSGG

168   model [11] is applied with 4 grey gases and 1 transparent gas ($\kappa_{g,0} = 0$).

169   Therefore, 5 RTEs, as shown in Eq.(2), have been solved, with the weighting

170   factors and the absorption coefficients for the gas as follows:

$$a_{g,i}(\vec{r}) = \sum_{j=1}^{N_c} c_{ij} \left(\frac{T_g(\vec{r})}{T_{ref}}\right)^{j-1}, i = 1, 2, \ldots, N_g, \ \ a_{g,0} = 1 - \sum_{i=1}^{N_g} a_{g,i}(\vec{r}) \quad (3)$$

$$\kappa_{g,i} = K_{g,i}P \left(Y_{\mathrm{H_2O}} + Y_{\mathrm{CO_2}}\right) \quad (4)$$

171   where c_{ij}, K_{gi} are the temperature dependent polynomial coefficients, N_c, N_g

172   are the number of polynomial coefficients and the number of grey gases,

173   respectively, P is the total pressure of the gas, and $Y_{\mathrm{H_2O}}, Y_{\mathrm{CO_2}}$ are the molar

174   fractions of $\mathrm{H_2O}$ and $\mathrm{CO_2}$, respectively.

175   The grey WSGG model is often used in combustion modelling. In this

176   case, the properties of the gas is represented by the effective absorption co-

177   efficient and the number of RTE solutions required is reduced to one. The

effective absorption coefficient of the grey gas is calculated from the total emissivity, ε, and path length, s, as [31]

$$\kappa_g = -\frac{1}{s}\ln(1 - \varepsilon) \tag{5}$$

where ε is determined by Eq. (1) with the path length, s, being considered as a mean beam length of the domain. The mean beam length is often determined from the volume of the domain, V, and the internal surface of the domain, A, as [32]

$$s = 3.6\frac{V}{A} \tag{6}$$

Using the mean beam length obtained from Eq. (6) for the grey WSGG model has been found to give considerably different heat flux results compared to those of the non-grey WSGG model in some cases [31, 33]. The RTE for the non-grey WSGG model, Eq. (2), is rewritten for the grey gas WSGG model, with the weighting factors for the gas and particles being unity, as

$$\frac{\mathrm{d}I\left(\vec{r}, \vec{s}\right)}{\mathrm{d}s} = -\left(\kappa_g(\vec{r}) + \kappa_p(\vec{r}) + \sigma_p(\vec{r})\right) I\left(\vec{r}, \vec{s}\right) + \kappa_g(\vec{r})I_{b,g}\left(\vec{r}\right) + E_p\left(\vec{r}\right)$$
$$+ \frac{\sigma_p(\vec{r})}{4\pi} \int_{4\pi} I\left(\vec{r}, \vec{s}\,'\right) \Phi\left(\vec{s}.\vec{s}\,'\right) \mathrm{d}\Omega' \tag{7}$$

The particle effects are accounted for in Eqs.(2) and (7) with equivalent absorption coefficient κ_p, scattering coefficient σ_p and the equivalent emission $E_{p,i}$ being defined as follows:

9

$$\kappa_p = \lim_{V \to 0} \sum_{n=1}^{N} Q_{abs,n} \frac{A_{p,n}}{V} \tag{8}$$

$$\sigma_p = \lim_{V \to 0} \sum_{n=1}^{N} Q_{sca,n} \frac{A_{p,n}}{V} \tag{9}$$

$$E_{p,i} = \lim_{V \to 0} \sum_{n=1}^{N} a_{pi,n} I_{bp,n} Q_{abs,n} \frac{A_{p,n}}{V} \tag{10}$$

where N is the number of particles within the volume V, $a_{pi,n}$ is the weighting factor for the ith grey gas, being determined from Eq. (3) with replacing T_g by the temperature of the nth particle $T_{p,n}$, $I_{bp,n}$ is the black body intensity at the temperature of particle n, and $A_{p,n}$ is the projected area of the nth particle. The summation over N particles is calculated during the particle tracks, where the number of particles is accounted for by the residence time of a trajectory through a control volume multiplied by the number of particles per second that trajectory represents. The particle radiative properties alter the heat exchange between the particles and the boundaries and gas phase, by modifying the radiation intensity field and affecting the heat available for convective transfer between the phases, which inherently modifies the gas temperature, combustion kinetics and fluid dynamics, which means that a fully coupled approach such as CFD is required to fully incorporate the impact of these properties on pollutant formation. The absorption efficiency $Q_{abs,n}$ and the scattering efficiency $Q_{sca,n}$ are calculated from the Mie theory [34] using the Planck mean values as follows:

$$Q_{abs,n}(T) = \frac{\int_0^\infty Q_{abs\lambda} e_{b\lambda}(T) \mathrm{d}\lambda}{\int_0^\infty e_{b\lambda}(T) \mathrm{d}\lambda} \tag{11}$$

10

$$Q_{sca,n}(T) = \frac{\int_0^\infty Q_{sca\lambda}e_{b\lambda}(T)\mathrm{d}\lambda}{\int_0^\infty e_{b\lambda}(T)\mathrm{d}\lambda} \tag{12}$$

where $e_{b\lambda}(T)$ is the spectral black body emissive power at the temperature T. $Q_{abs\lambda}$ and $Q_{sca\lambda}$ are spectral absorption and scattering efficiencies of a particle at wavelength λ, respectively.

In this study, the high degree of forward scattering of the particles was treated by using a so-called zero-order delta Eddington function, which applies a modified scattering efficiency scaled by the asymmetry factor, g as in [32, 35], $Q_{sca,n}^* = (1 - g)Q_{sca,n}$. The optical constants used for the calculation of the refractive index of the coal particles were taken from experimental measurements for the Kentucky No. 9 coal, with the real part n=1.8 and the wavelength-dependent k determined within the spectral range 2-20 μm [36]. For the fly-ash particles, the wavelength-dependent optical constants measured by Goodwin [37], as parametrised by Liu and Swithenbank [38], were used. The Planck mean coefficients were pre-calculated for a range of diameters and temperatures of the particles. For each calculation of the coal and fly ash particles, the $Q_{abs,n}$ and $Q_{sca,n}$ values were obtained by employing linear interpolation. The radiative properties of the burning particles are also linearly interpolated between the coal and fly ash values based on the current mass of the char in the burning particles.

Two other approaches for the particle radiative properties were also investigated and compared to the Planck mean coefficients, namely the constant and the linear-function values. In terms of constant values, a particle absorption efficiency value of 0.9 [16, 23, 39, 40] and a particle scattering factor 0.6 [23, 39] for both air-fired and oxy-fired conditions are employed. The

11

particle scattering efficiency is calculated from the scattering factor, f_p, as $Q_{sca} = (1 - f_p)(1 - Q_{abs})$, resulting in a constant scattering efficiency of 0.04. For the linear-function value, the radiative properties of particles vary as linear functions of the mass fraction of char and volatiles in the particles. The linear emissivity function [41], as shown in Eq. (13), and the linear function scattering factor [42], as shown in Eq. (9), are used as follows:

$$\epsilon_p = X_c + 0.6 \left(1 - X_c\right) \tag{13}$$

$$f_p = 0.9 X_{v,c} + 0.6 \left(1 - X_{v,c}\right) \tag{14}$$

where X_c is the fraction of unburnt char mass, and $X_{v,c}$ is the fraction of unburnt combustibles.

2.2. NOx formation

In pulverised coal combustion, the NO_x emissions consists mostly of NO, with much lower amounts of N_2O and NO_2 [43, 44]. Therefore, only NO formation and destruction are mentioned in this study. Existing sub-models for predicting NO emissions, which have been developed for conventional air combustion, are employed in modelling for both the air- and oxy-fired conditions. Previous studies have shown that the NO formation and reduction mechanisms in oxyfuel combustion are fundamentally similar to those in air condition [45–47]. Significant contributions to NO formation can result from four mechanisms: fuel-NO, thermal-NO, prompt-NO and N_2O mechanisms. The fuel-NO mechanism is the dominant source of NO formation in coal-fired systems, being responsible for approximately more than 80% of the total NO

formation [44, 48, 49], while the formation from the prompt-NO and N_2O mechanisms can often be neglected [50]. The NO destruction includes a reburning mechanism and the heterogeneous reaction of NO with the carbon atoms on the char surface. Fig. 1 illustrates a simple NO formation and destruction pathway that is employed in this paper.

The fuel-NO mechanism occurs from the oxidation of fuel-bound nitrogen which is released from the fuel devolatilisation, called volatile-N, and the nitrogen remains in the char, called char-N. The volatile-N converts to intermediate nitrogen compounds, primarily HCN and NH_3, which are then oxidised to form NO. The char-N converts directly to NO from oxidised char-N atoms or partly converts to intermediate nitrogen compounds which is then converted partially to NO. As a results, the formation from char-N is proportional to the carbon burnout. The volatile-N is dominant of NO formation due to 70-90% of coal nitrogen converts to volatile under the devolatilisation precess [17, 51] and 60-80% of NO formation from the volatile-N in regular pulverised coal combustion [51, 52].

Thermal-NO is formed from the oxidation of atmospheric nitrogen in relatively high-temperature environment and this mechanism is strongly temperature dependent. The formation of NO under this mechanism is described by the extended Zeldovich mechanism. Themal-NO occurs in air-coal combustion and can result in about 25% of the total NO emission [53], and this mechanism is almost eliminated under oxy-fired condition where nitrogen is replaced by CO_2. The reactions governing the formation of the thermal-NO mechanism are expressed as follows:

$$O + N_2 \rightleftharpoons N + NO \tag{R3}$$

$$N + O_2 \rightleftharpoons O + NO \tag{R4}$$

$$N + OH \rightleftharpoons H + NO \tag{R5}$$

The net rate of thermal-NO formation is expressed as

$$\frac{d[NO]}{dt} = k_{f1}[O][N_2] + k_{f2}[N][O_2] + k_{f3}[N][OH] \tag{15}$$
$$-k_{r1}[NO][N] - k_{r2}[NO][O] - k_{r3}[NO][H]$$

where k_{f1}, k_{f2}, k_{f3} are the rate constants for the forward reactions (R3)-(R5), respectively. The rate constants for the reverse reactions are k_{r1}, k_{r2}, k_{r3}. The forward and reverse rates from this study were employed from [54] as shown in Table 3.

When assuming that the rate of consumption of free N atoms becomes equal to the rate of its formation, the overall rate for the three reversible reactions (R3)-(R5) can be expressed as [55]

$$\frac{d[NO]}{dt} = 2[O] \left(\frac{k_{f1}[N_2] - \frac{k_{r1}k_{r2}[NO]^2}{k_{f2}[O_2]}}{1 + \frac{k_{r1}[NO]}{k_{f2}[O_2] + k_{f3}[OH]}} \right) \tag{16}$$

The concentration of O and OH atoms can be estimated using equilibrium or partial equilibrium assumptions.

The NO destruction mechanisms occur when NO reactions with CH_i radicals, named reburning, and the heterogeneous reaction of NO with the carbon atoms on the char surface. The destruction mechanisms are expressed

by a general reaction (R6) and heterogeneous reaction (R7), respectively, as follows:

$$CH_i + NO \xrightarrow{k_i} HCN + ... \tag{R6}$$

$$Char + NO \xrightarrow{k_{char}} N_2 + ... \tag{R7}$$
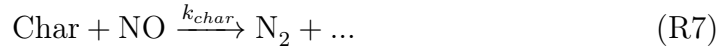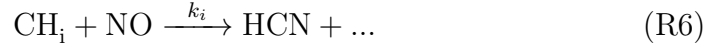
where CH_i are the hydrocarbon species, i=1, 2, or 3, depending on the hydrocarbons used in the flame, and k_i and k_{char} are the rate constants for reactions (R6) and (R7), respectively.

In this paper, 80% of the coal nitrogen is assumed to be released with the volatiles-N and 20% of the nitrogen is bound with char. The volatile-N converts to HCN and NH_3 as intermediate species at 55% and 10%, respectively, with the rest of the volatile-N forms directly to NO. A similar partition of the intermediate species has been examined on a pulverised coal combustion and showed a good agreement with the experiment data [56]. The char-N is directly converted to NO [57]. The partial equilibrium approach [58] was selected for the reburning solution with CH_4 selected as the best equivalent fuel after examining different equivalent fuels CH_i (i=1-4).

2.3. Measurement techniques and methods

The PACT 250 kW air/oxy-fired CTF was designed with detailed measurement and characterisation capabilities, and a range of techniques were used to obtain a detailed assessment of the oxyfuel combustion process. The experimental data obtained from measurement for air-fired condition and different cases of oxy-fired conditions, such as Oxy-27, Oxy-30, were used to evaluate the CFD study results.

15

The concentration of NO was measured at different regions within the furnace and at the exit section of the furnace using a Signal 4000VMA chemiluminescence analyser which is based on the chemiluminescent gas phase reaction between ozone and nitric oxide to give nitrogen dioxide and oxygen. Approximately 10% of the NO_2 produced emission of a photon, varying in wavelength between 0.6 and 0.3 micrometres. The intensity of this emission is proportional to the mass flow rate of NO and is measured by a photomultiplier tube.

3. Results and discussion

3.1. Effect of radiative properties of the mixture

Fig. 2 shows the radial distribution of the temperature at different positions along the furnace for both air- and oxy-fired conditions. Different cases are implemented by employing the grey or non-grey gas radiative models coupled with the constant, linear or Planck averaged coefficients for the radiative properties of the particles. In terms of having the same radiative model for the gases (grey WSGG or non-grey WSGG), there is only a small difference in the temperature distribution between the cases that have constant and linear radiative properties for the particles. In contrast, being described by the same radiative model for the particles (constant or linear cases), the non-grey gas models show higher temperature results than that of the grey gas models, mainly in regions containing a higher particle concentration (such as the inner recirculation zone located close to the exit of the burner) as shown in Fig. 3. Temperature results for the case of the non-grey gas and the Planck mean values for the particles (NGWSGG-Mie) is higher than cases

16

having constant or linear radiative coefficients for the particles (NGWSGG-Const, NGWSGG-Linear). This is due to the radiative properties of the particles being described by the Mie theory being the dominant scattering coefficients and having significantly lower absorption coefficients, as shown in Fig. 4, and consequently reducing the radiative heat loss from the particle, and increasing convective heat transfer from the particles to the surrounding gas. Applying the same value for the absorption efficiency of 0.9 for both the coal/char and ash in the constant model results in a significantly higher absorption coefficient compared to that of the Mie theory, which calculates absorption efficiencies of coal and fly ash separately. The Mie theory values provide significantly lower absorption efficiency for the fly ash particles, which, according to the limited published data on optical constant values for coal and fly ash, is more physically reasonable.

In the near-burner region, the higher concentration of the particles in the internal recirculation zone also causes a significantly higher in-flame temperature of the non-grey WSGG cases than for the other cases described by the grey gas model, while this is not found to be the situation in the outer recirculation zone, where there is a lower concentration of particles. Further downstream, at an axial distance of 575 mm from the exit of the burner, where there is a substantial amount of fly ash with steady concentrations in the radial direction, there is no fluctuation in the difference of the radial temperature profiles. A similar variation trend can be seen at 3500 mm from the exit of the burner in the burnout region. However, there is a similar temperature distribution for all cases investigated in this region. The contours of the temperature distribution for both the air-fired and oxy-fired conditions

17

are shown in Fig. 5. From these figures, the high-temperature flame of the oxy-fired conditions are more close to the centre line of the furnace compared to that of the air-fired condition. This can be a consequence of the lower volume flow rate of oxidant flows under the oxy-fired conditions compared to that of the air-fired condition.

The results of this CFD study for the radiative incident wall heat fluxes are shown in Fig. 6 for both air and oxy-fired conditions compared to experimental data from [23]. The experimental data show that the incident wall heat fluxes increase quickly in the first section of the furnace, reaching their peak values at about 0.5 m and 0.75 m from the burner exit for air and oxy-fired conditions, respectively. The difference in the peak value's position of the incident wall heat flux under the oxy-fired condition compared to that of the air-fired condition can be explained by the different flame behaviour under conditions investigated in this study, with the lower volume flow rates of the inlet flows under oxyfuel conditions. The behaviour of the heat fluxes are quite similar for both conditions in the downstream region of the furnace from the axial distance of 1 m to the furnace exit. Results from CFD show the same behaviours of incident wall heat fluxes compared to experimental data for both conditions. The different flame behaviour, shown in Fig. 5, can explain the differences in the peak positions of the heat fluxes for two conditions. In terms of the effects of the gas and particle models to incident wall heat fluxes under the CFD study for both air and oxy-fired conditions, the non-grey gas model shows an improvement for the results in the flame zone compared to that of the grey gas model. The GWSGG-const case and the NGWSGG-Const case show over-predicted results in comparison with the

18

cases having linear coefficients for the particle radiation, namely GWSGG-Linear and the NGWSGG-Linear. This is due to the reducing equivalent absorption coefficients of the particles under the linear properties of the particles. The properties of the particles described by the Mie theory results in a significantly lower incident wall heat flux but a much closer agreement with the experimental data. The lower incident wall radiation is due to the Mie theory cases showing a significantly lower equivalent absorption coefficient and higher scattering efficient of the particles compared to the constant and linear cases, as shown in Fig. 4.

3.2. Effect of radiative properties on the NOx emission

The radial and central profiles of the NO concentration from the measurement and CFD modelling for both the air- and oxy-fired conditions are shown in Figs. 7 and 8, respectively. Experimental data for the cases investigated in this study show that the NO concentration in the region close to the burner in the air case is significantly higher than that in the oxy-fired conditions. Under the oxy-fired conditions, the NO concentration at the burner exit, Fig. 9, decreases by about 25% for the Oxy-27 and 30% for Oxy-30 cases compared to that of the air case. Because of the combustion in this study using once-through O_2/CO_2 mixtures, without recycled flue gas, the lower NO under the oxyfuel conditions can be explained by the missing nitrogen and potentially enhanced heterogeneous reburning because of the higher CO concentration [59], as the CO concentrations are higher under Oxy-27, and higher still under Oxy-30 conditions [23]. In terms of CFD modelling, the influence of the NGWSGG and Mie theory values on NO prediction are investigated in comparison with the standard approach for coal combustion

19

modelling (GWSGG-Const). The influence of the choice of particle models on the prediction of NO emissions are also investigated. Because of the similar effect of the constant and the linear models of particles on the radiative heat transfer, as shown in Section 3.1, the constant model is selected to compare to the Mie model. Figs. 7 and 8 show a comparison of the predicted NO concentrations under two cases, the GWSGG-Const and NGWSGG-Mie cases. Both sets of results show a similar trend and a reasonable agreement with the experimental measurements, except in the inner recirculation zone close to the burner. Although the NO formation/destruction mechanisms employed for the oxyfuel cases in this study were originally developed for air conditions, the NO prediction results for the oxy-fired cases show much closer agreement with the measurements than for the air-fired case. In the inner recirculation zone close to the burner, the NO distribution under the NGWSGG-Mie case shows a better trend compared to that of the GWSGG-Const case, with a significantly higher NO concentration. This can be due to the higher temperature in the NGWSGG-Mie case subsequent to the other changes in the combustion behaviour in this region, for example the lower volatile concentration as shown in Fig. 10. The higher difference of NO concentration of the two cases for both the air and oxyfuel conditions at 200 mm compared to that at 75 mm and 575 mm can be explained by the higher difference in the temperature of the two cases at this section. And this can be seen more clearly in the oxyfuel case compared to the air case. Results from the experiment and simulation, Fig. 9, show the same trend that the NO concentration at the exit section of the air-fuel condition is higher than that of the oxy-conditions. Under the air conditions, Fig. 9(a), the NGWSGG-

20

Mie case results in a significant increase in the exit NO concentration, with a 21% increase compared with the experimental measurement, while the disagreement is only 9.7% for the GWSGG-Const case. These differences are much lower under the oxyfuel conditions as shown in Fig. 9(b). The higher difference in the NO concentration between the NGWSGG-Mie case compared to the GWSGG-Const under the air-fired condition compared to those under the oxy-fired conditions can be explained by the NO formation from the thermal mechanism, and this is almost eliminated under the oxy-fired conditions.

4. Summary and Conclusions

This study has focused on the radiative properties of the particles for both air-fired and oxy-fired coal combustion conditions, and the impact of modelling these properties on the calculated predictions of the NO pollutants. The grey and non-grey gas property models coupled with different solutions for the particle properties are employed to describe the radiation heat transfer and these results are compared against experimental data. The radiative properties of the particles described by the Mie theory show a significant improvement in the incident wall heat flux. However, the temperature is much higher compared to the case of having constant properties for the particles in the inner recirculation region having higher coal/char particle concentration. Further studies need to focus on the influence of the radiation models on combustion behaviours in the burner region, such as flame ignition and particle combustion. This study is performed only on a pilot-scale facility so the influence of the radiation models on large-scale furnace needs to be

21

investigated.

The non-grey WSGG coupled with the Mie theory results in a considerable improvement in the NO prediction in the burner region where containing a high particle concentration of the coal/char particles, compared to those from the simplified models for the gases and the particles. However, these models show an over prediction of the NO concentrations at the exit section of the furnace, especially for the air-fuel case. NO_x predictions can vary by as much as 10% depending on choice of radiation model, due to the sensitivity of the thermal NO_x mechanism, although this is somewhat reduced when considering oxy-fired conditions. Accurate radiation modelling needs to consider simultaneously the effects of other accurate sub-models in the prediction of the NO formation, such as turbulence and chemical reaction models. The importance of the heterogeneous reburning due to CO also needs to be investigated as a potential addition to the current mechanism for application to oxyfuel conditions.

5. Acknowledgements

Nomenclature

$a_{g,i}$ emissivity weighting factor for the gas   -

$a_{pi,n}$ emissivity weighting factor for the nth particle   -

A_p projected surface area of the particle   (m^2)

A_r pre-exponential factor   (1/s)

$c_{i,j}$ temperature dependent polynomial coefficients   -

$e_{b\lambda}(T)$ spectral black body emissive power   (W/(m^2.µm))

E_a activation energy   (J/kmol)

$E_{p,i}$ emision of the particles corresponding to the ith grey gas   (W/m^3)

f_p scattering factor of particle   -

g asymmetry factor   -

$I_i\left(\vec{r},\vec{s}\right)$ radiative intensity of grey gas i^{th} at position $\vec{r}$ in direction $\vec{s}$ (W/(m^2.sr))

$I_{b,g}\left(\vec{r}\right)$ black body intensity of grey gas at position $\vec{r}$ (W/(m^2.sr))

$I_{bp,n}$ black body intensity of grey particle   (W/(m^2.sr))

$k_{g,i}$ absorption coefficient of the ith grey gas   (m^{-1})

κ_p equivalent absorption coefficient of particles   (m^{-1})

$K_{g,i}$ temperature dependent polynomial coefficients   -

N number of particles go through volume V -

N_c number of polynomial coefficients   -

N_g number of grey gases   -

P total pressure of gas   (bar)

Q_{abs} absorption efficiency of particles   -

Q_{sca} scattering efficiency of particles   -

Q_{sca}^* effective scattering efficiency of particles   -

$Q_{abs\lambda}$ spectral absorption efficiency of particles at wavelength λ -

23

506 $Q_{sca\lambda}$ spectral scattering efficiency of particles at wavelength λ -

507 R universal gas constant   (J/kmol.K)

508 T_g temperature of gas   (K)

509 T_p temperature of particle   (K)

510 T_{ref} reference temperature   (K)

511 V volume   (m^3)

512 $Y_{\mathrm{H_2O}}$ mole fraction of H_2O -

513 $Y_{\mathrm{CO_2}}$ mole fraction of CO_2 -

514

515 **Greek symbols**

516 β temperature exponential   -

517 ε emissivity of gas mixture   -

518 ε_p emissivity of particle   -

519 λ wavelength   µm

520 σ_p equivalent scattering coefficient of particles   (1/m)

521 Φ scattering phase function   -

522 Ω' solid angle   (sr)

24

References

[1] British Petroleum, BP Statistic Review of World Energy, June 2017.

[2] K. Andersson, R. Johansson, F. Johnsson, Thermal radiation in oxy-fuel flames, International Journal of Greenhouse Gas Control 5 (2011) S58–S65.

[3] R. Viskanta, M. Menguc, Radiative transfer in dispersed media, Applied Mechanics Reviews 42 (9) (1989) 241–259.

[4] L. Chen, S. Z. Yong, A. F. Ghoniem, Oxy-fuel combustion of pulverized coal: characterization, fundamentals, stabilization and CFD modeling, Progress in Energy and Combustion Science 38 (2) (2012) 156–214.

[5] C. Yin, J. Yan, Oxy-fuel combustion of pulverized fuels: Combustion fundamentals and modeling, Applied Energy 162 (2016) 742–762.

[6] H. Hottel, A. Sarofim, Radiative transfer, McGraw-Hill, New York.

[7] M. F. Modest, The weighted-sum-of-gray-gases model for arbitrary solution methods in radiative transfer, Journal of Heat Transfer 113 (3) (1991) 650–656.

[8] T. Smith, Z. Shen, J. Friedman, Evaluation of coefficients for the weighted sum of gray gases model, Journal of Heat Transfer 104 (4) (1982) 602–608.

[9] C. Yin, L. C. Johansen, L. A. Rosendahl, S. K. Kær, New weighted sum of gray gases model applicable to computational fluid dynamics

25

544 (CFD) modeling of oxy- fuel combustion: derivation, validation, and
545 implementation, Energy & Fuels 24 (12) (2010) 6275–6282.

546 [10] R. Johansson, B. Leckner, K. Andersson, F. Johnsson, Account for vari-
547 ations in the H_2O to CO_2 molar ratio when modelling gaseous radiative
548 heat transfer with the weighted-sum-of-grey-gases model, Combustion
549 and Flame 158 (5) (2011) 893–901.

550 [11] T. Kangwanpongpan, F. H. França, R. C. da Silva, P. S. Schneider,
551 H. J. Krautz, New correlations for the weighted-sum-of-gray-gases model
552 in oxy-fuel conditions based on HITEMP 2010 database, International
553 Journal of Heat and Mass Transfer 55 (25) (2012) 7419–7433.

554 [12] L. Rothman, I. Gordon, R. Barber, H. Dothe, R. Gamache, A. Goldman,
555 V. Perevalov, S. Tashkun, J. Tennyson, HITEMP, the high-temperature
556 molecular spectroscopic database, Journal of Quantitative Spectroscopy
557 and Radiative Transfer 111 (15) (2010) 2139–2150.

558 [13] R. Viskanta, M. Mengüç, Radiation heat transfer in combustion systems,
559 Progress in Energy and Combustion Science 13 (2) (1987) 97–160.

560 [14] R. Johansson, B. Leckner, K. Andersson, F. Johnsson, Influence of par-
561 ticle and gas radiation in oxy-fuel combustion, International Journal of
562 Heat and Mass Transfer 65 (2013) 143–152.

563 [15] W. Grosshandler, S. Monteiro, Attenuation of thermal radiation by pul-
564 verized coal and char, Journal of Heat Transfer 104 (4) (1982) 587–593.

565 [16] R. Backreedy, L. Fletcher, L. Ma, M. Pourkashanian, A. Williams,

566 Modelling pulverised coal combustion using a detailed coal combustion
567 model, Combustion Science and Technology 178 (4) (2006) 763–787.

568 [17] S. Hill, L. D. Smoot, Modeling of nitrogen oxides formation and de-
569 struction in combustion systems, Progress in Energy and Combustion
570 Science 26 (4) (2000) 417–458.

571 [18] A. Williams, M. Pourkashanian, P. Bysh, J. Norman, Modelling of coal
572 combustion in low-NO_x pf flames, Fuel 73 (7) (1994) 1006–1019.

573 [19] L. Chen, A. F. Ghoniem, Simulation of oxy-coal combustion in a 100
574 kWth test facility using RANS and LES: a validation study, Energy &
575 Fuels 26 (8) (2012) 4783–4798.

576 [20] T. Kangwanpongpan, R. C. da Silva, H. J. Krautz, Prediction of oxy-coal
577 combustion through an optimized weighted sum of gray gases model,
578 Energy 41 (1) (2012) 244–251.

579 [21] C. Yin, Nongray-gas effects in modeling of large-scale oxy–fuel combus-
580 tion processes, Energy & Fuels 26 (6) (2012) 3349–3356.

581 [22] J. Zhang, T. Ito, S. Ito, D. Riechelmann, T. Fujimori, Numerical inves-
582 tigation of oxy-coal combustion in a large-scale furnace: non-gray effect
583 of gas and role of particle radiation, Fuel 139 (2015) 87–93.

584 [23] X. Yang, A. Clements, J. Szuhánszki, X. Huang, O. F. Moguel, J. Li,
585 J. Gibbins, Z. Liu, C. Zheng, D. Ingham, et al., Prediction of the ra-
586 diative heat transfer in small and large scale oxy-coal furnaces, Applied
587 Energy 211 (2018) 523–537.

27

[24] A. G. Clements, S. Black, J. Szuhánszki, K. Stęchły, A. Pranzitelli, W. Nimmo, M. Pourkashanian, LES and RANS of air and oxy-coal combustion in a pilot-scale facility: predictions of radiative heat transfer, Fuel 151 (2015) 146–155.

[25] B. Launder, G. J. Reece, W. Rodi, Progress in the development of a Reynolds-stress turbulence closure, Journal of Fluid Mechanics 68 (03) (1975) 537–566.

[26] A. German, T. Mahmud, Modelling of non-premixed swirl burner flows using a Reynolds-stress turbulence closure, Fuel 84 (5) (2005) 583–594.

[27] F. Breussin, F. Pigari, R. Weber, Predicting the near-burner-one flow field and chemistry of swirl-stabilied low-NO_x flames of pulveried coal using the RNG-k-ε, RSM and k-ε turbulence models, in: Symposium (International) on Combustion, Vol. 26, Elsevier, 1996, pp. 211–217.

[28] S. Badzioch, P. G. Hawksley, Kinetics of thermal decomposition of pulverized coal particles, Industrial & Engineering Chemistry Process Design and Development 9 (4) (1970) 521–530.

[29] I. Smith, The combustion rates of coal chars: A review, Symposium (International) on Combustion 19 (1) (1982) 1045–1065.

[30] A. Pranzitellia, Development and application of a novel f radiation property model for oxy-coal combustion, in: Oxyfuel combustion conference, Vol. 3, 2013.

[31] G. Krishnamoorthy, A comparison of gray and non-gray modeling approaches to radiative transfer in pool fire simulations, Journal of Hazardous Materials 182 (1) (2010) 570–580.

[32] M. F. Modest, Radiative Heat Transfer, Academic press, 2003.

[33] P. Nakod, G. Krishnamoorthy, M. Sami, S. Orsino, A comparative evaluation of gray and non-gray radiation modeling strategies in oxy-coal combustion simulations, Applied Thermal Engineering 54 (2) (2013) 422–432.

[34] C. F. Bohren, D. R. Huffman, Absorption and scattering of light by small particles, Wiley science paperback series. Wiley, 1983.

[35] F. Liu, E. Garbett, J. Swithenbank, Effects of anisotropic scattering on radiative heat transfer using the P1-approximation, International Journal of Heat and Mass Transfer 35 (10) (1992) 2491–2499.

[36] S. Manickavasagam, M. Menguc, Effective optical properties of pulverized coal particles determined from FT-IR spectrometer experiments, Energy & Fuels 7 (6) (1993) 860–869.

[37] D. Goodwin, M. Mitchner, Measurements of the near infrared optical properties of coal slags, Chemical Engineering Communications 44 (1-6) (1986) 241–255.

[38] F. Liu, J. Swithenbank, The effects of particle size distribution and refractive index on fly-ash radiative properties using a simplified approach, International Journal of Heat and Mass Transfer 36 (7) (1993) 1905–1912.

29

[39] L. Ma, M. Gharebaghi, R. Porter, M. Pourkashanian, J. Jones, A. Williams, Modelling methods for co-fired pulverised fuel furnaces, Fuel 88 (12) (2009) 2448–2454.

[40] M. N. Borjini, K. Guedri, R. Saïd, Modeling of radiative heat transfer in 3D complex boiler with non-gray sooting media, Journal of Quantitative Spectroscopy and Radiative Transfer 105 (2) (2007) 167–179.

[41] E. Chui, P. M. Hughes, G. Raithby, Implementation of the finite volume method for calculating radiative transfer in a pulverized fuel flame, Combustion Science and Technology 92 (4-6) (1993) 225–242.

[42] C. Yin, On gas and particle radiation in pulverized fuel combustion furnaces, Applied Energy 157 (2015) 554–561.

[43] R. Boardman, C. Eatough, G. Germane, L. Smoot, Comparison of measurements and predictions of flame structure and thermal NO_x, in a swirling, natural gas diffusion flame, Combustion Science and Technology 93 (1) (1993) 193–210.

[44] A. Eaton, L. Smoot, S. Hill, C. Eatough, Components, formulations, solutions, evaluation, and application of comprehensive combustion models, Progress in Energy and Combustion Science 25 (4) (1999) 387–436.

[45] B. Dhungel, J. Maier, G. Scheffknecht, Emission behaviour during oxy-coal combustion, in: AIchE 2007 Annual Meeting, Salt Lake City, UT, 2007.

[46] G. Scheffknecht, L. Al-Makhadmeh, U. Schnell, J. Maier, Oxy-fuel coal

654   combustion-A review of the current state-of-the-art, International Jour-
655   nal of Greenhouse Gas Control 5 (2011) S16–S35.

[47] R. Stanger, T. Wall, R. Spoerl, M. Paneru, S. Grathwohl, M. Weidmann,
G. Scheffknecht, D. McDonald, K. Myöhänen, J. Ritvanen, et al., Oxy-
fuel combustion for CO_2 capture in power plants, International Journal
of Greenhouse Gas Control 40 (2015) 55–125.

[48] P. F. Nelson, A. N. Buckley, M. D. Kelly, Functional forms of nitrogen
in coals and the release of coal nitrogen as NO_x precursors (HCN and
NH_3), Vol. 24, Elsevier, 1992, pp. 1259–1267.

[49] L. D. Smoot, P. J. Smith, Coal combustion and gasification, Springer
Science & Business Media, US, 2013.

[50] P. Coelho, M. Carvalho, Mathematical modelling of NO formation in
a power station boiler, Combustion Science and Technology 108 (4-6)
(1995) 363–382.

[51] N. Spitz, R. Saveliev, E. Korytnyi, M. Perelman, E. Bar-Ziv, B. Chud-
novsky, Prediction of performance and pollutant emission from pulver-
ized coal utility boilers, Nova Science Publishers, Inc., Hauppauge, NY,
2007.

[52] J. H. Pohl, A. F. Sarofim, Devolatilization and oxidation of coal nitrogen,
in: Symposium (International) on Combustion, Vol. 16, Elsevier, 1977,
pp. 491–501.

[53] P. Edge, M. Gharebaghi, R. Irons, R. Porter, R. Porter, M. Pourkasha-
nian, D. Smith, P. Stephenson, A. Williams, Combustion modelling

opportunity and challenges for oxy-coal carbon capture technology, Chemical Engineering Research and Design 89 (9) (2011) 1470–1493.

[54] R. K. Hanson, S. Salimian, Survey of rate constants in the N/H/O system, in: Combustion chemistry, Springer, 1984, pp. 361–421.

[55] C. T. Bowman, Kinetics of pollutant formation and destruction in combustion, Progress in Energy and Combustion Science 1 (1) (1975) 33–45.

[56] B. Alganash, M. C. Paul, I. A. Watson, Numerical investigation of the heterogeneous combustion processes of solid fuels, Fuel 141 (2015) 236–249.

[57] A. Arenillas, R. Backreedy, J. Jones, J. Pis, M. Pourkashanian, F. Rubiera, A. Williams, Modelling of NO formation in the combustion of coal blends, Fuel 81 (5) (2002) 627–636.

[58] N. Kandamby, G. Lazopoulos, F. Lockwood, A. Perera, L. Vigevano, Mathematical modeling of NO_x emission reduction by the use of reburn technology in utility boilers, ASME Internationational Joint Power Generation Conference and Exhibition, Houston, Texas, 1996.

[59] H. Liu, R. Zailani, B. M. Gibbs, Comparisons of pulverized coal combustion in air and in mixtures of O_2/CO_2, Fuel 84 (7) (2005) 833–840.

Table 1

Properties of El-Cerrejon coal.*

Proximate analysis (AR, wt.%)				Ultimate analysis (DAF, wt.%)					GCV(AR)
Fixed carbon	Volatiles	Ash	Moisture	C	H	N	S	O**	(MJ/kg)
53.98	35.50	2.9	7.63	80.92	5.12	1.65	0.52	11.79	29.61

* AR, as received; DAF, dry ash-free.

** Calculated by difference.
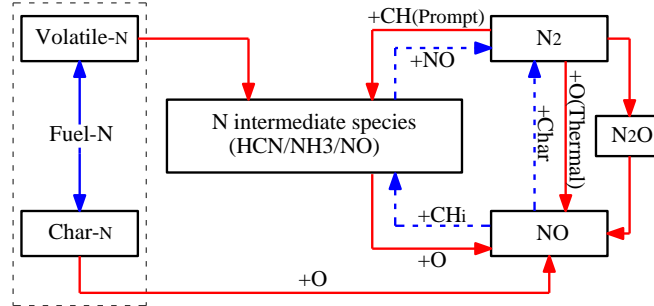
Fig. 1: Pathway of NOx formation/destruction employed in the CFD prediction of NO pollutant.

Table 2

Inlet flow rates, temperature and gas concentrations that were employed for CFD calculation of the three cases (Air, Oxy-27 and Oxy-30). The balance of gas compositions for the primary, secondary and tertiary gas streams in the oxyfuel cases was CO_2.

	Air	Oxy-27	Oxy-30
Mass flow rate (kg/h)			
Coal	25.71	25.71	25.71
Primary	63.6	60.90	54.85
Secondary	92.2	87.77	78.00
Tertiary	158.4	150.73	133.96
Inlet gas temperature (K)			
Primary	297.15	294.95	294.95
Secondary	524.65	525.15	525.15
Tertiary	524.65	525.15	525.15
Oxygen concentration (mass%)			
Primary	23.15	16.20	16.20
Secondary	23.15	22.50	25.71
Tertiary	23.15	22.50	25.71

Table 3 Reaction rate coefficients in the form $k = A_r T^{\beta} \exp\left(-E_a/RT\right)$ [54].

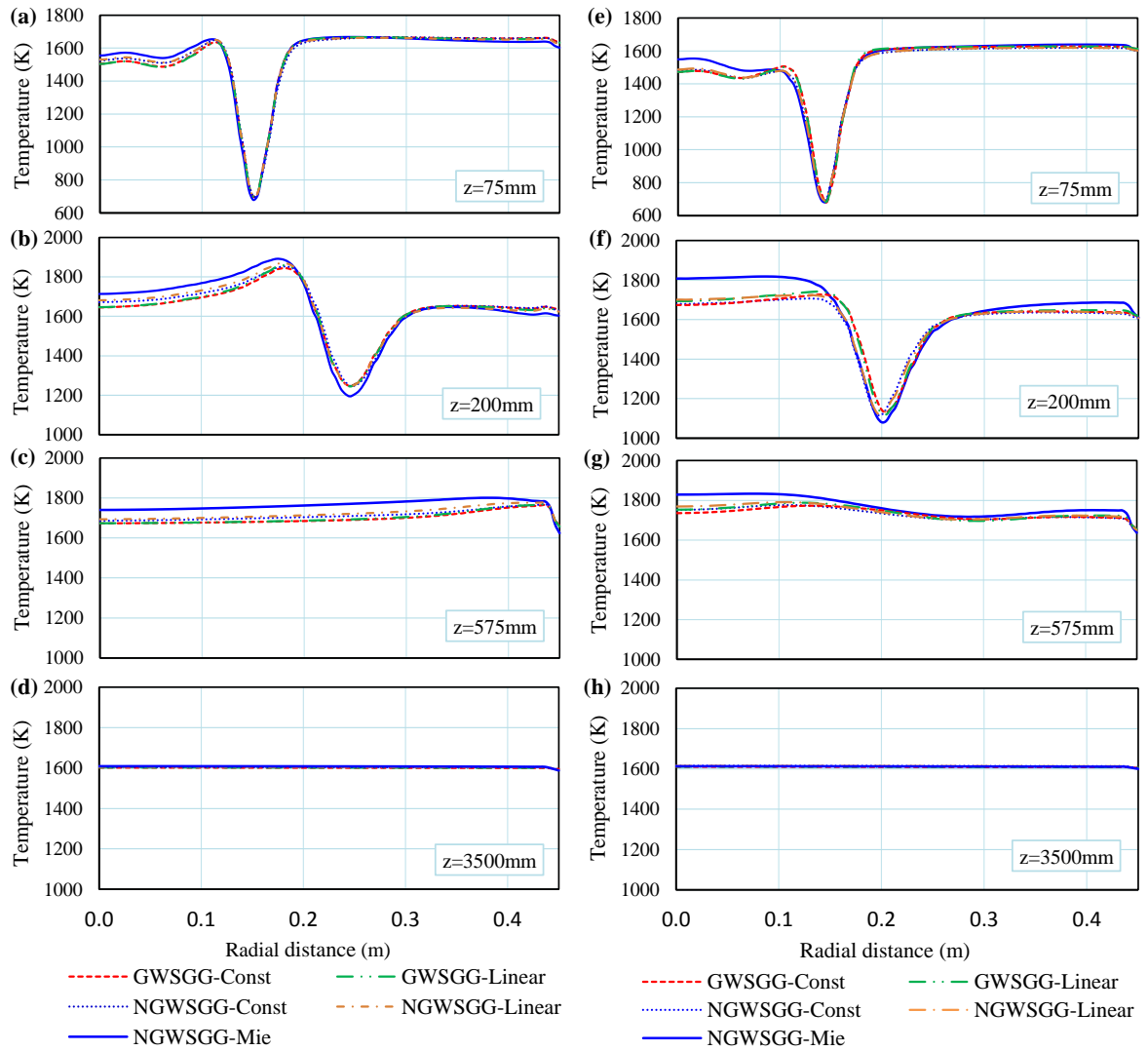| Reaction constant	A_r (m³/kmol-s)	β	E_a (J/kmol)
k_{f1}	1.80×10^{11}	0	3.19×10^8
k_{f2}	1.80×10^7	1	3.89×10^7
k_{f3}	7.10×10^{10}	0	3.74×10^6
k_{r1}	3.80×10^{10}	0	3.53×10^6
k_{r2}	3.80×10^6	1	1.73×10^8
k_{r3}	1.70×10^{11}	0	2.04×10^8

Fig. 2: Radial temperature distribution at several distances from the burner exit for the air-fired condition (a-d) and oxy-27 condition (e-h).
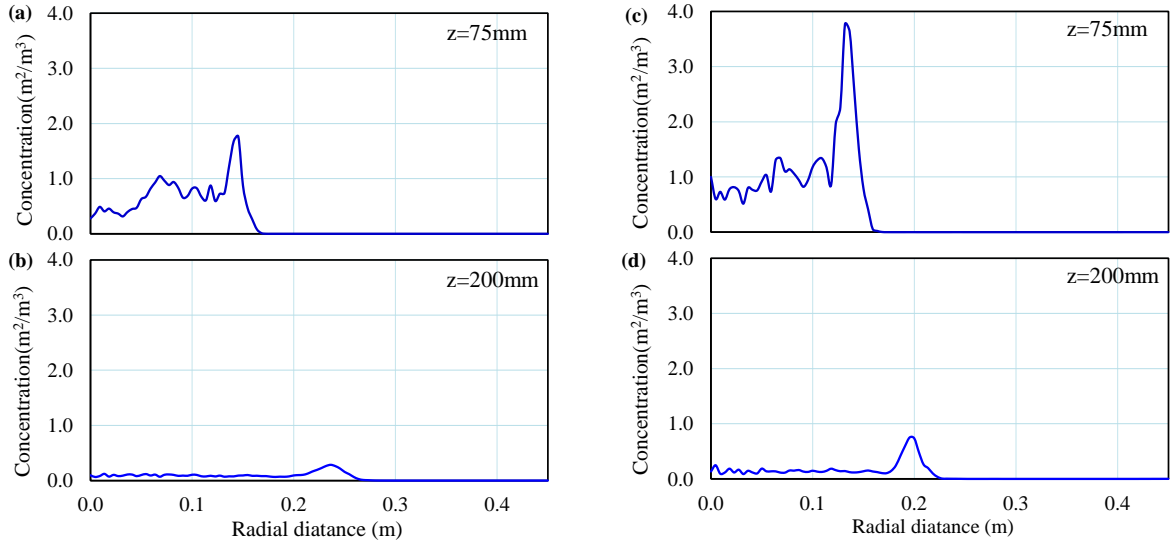
Fig. 3: Projected surface area distributions of coal/char particles calculated from NGWSGG-Mie cases at distances 75mm and 200mm from the burner exit for (a, b) air-fired condition and (c, d) Oxy-27 condition.
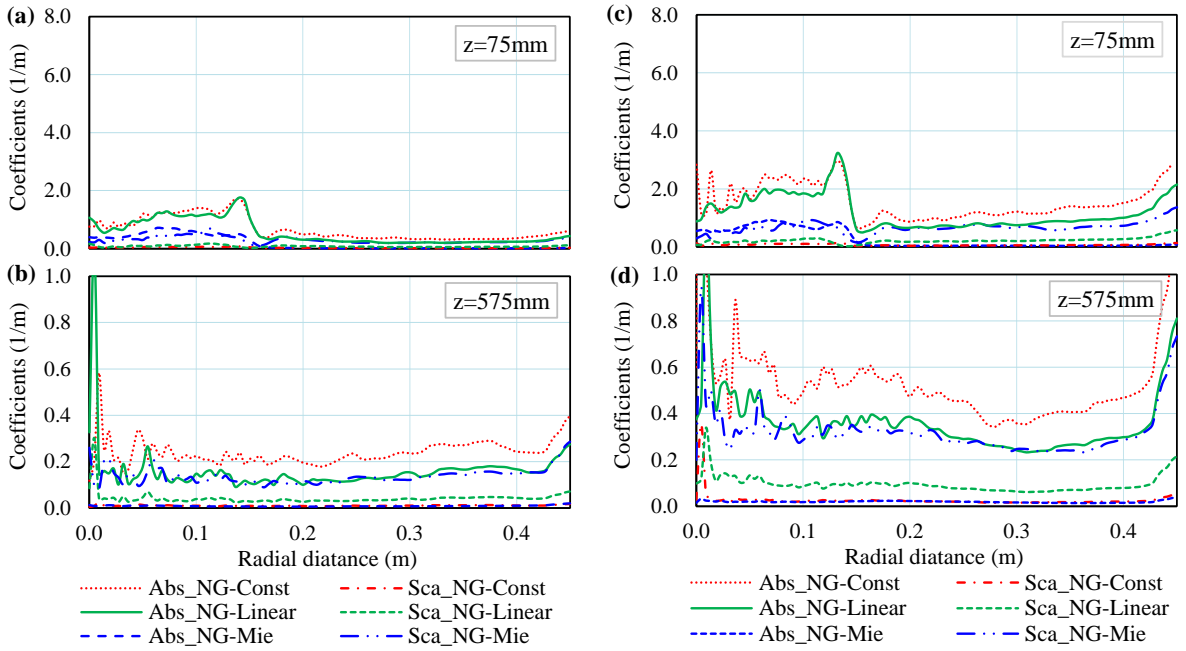

Fig. 4: Particles radiative properties at distances 75 mm and 575 mm from the burner exit for (a, b) air-fired condition, and (c, d) oxy-27 condition.
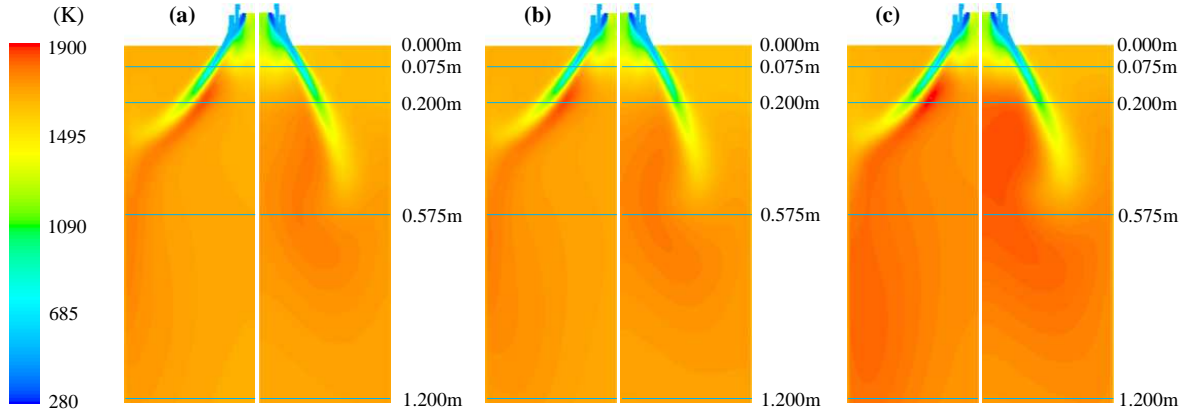
Fig. 5: Temperature distributions of the air-fired condition (left) and Oxy-27 condition (right) for different radiative properties of the gas and particles. (a)WSGG-Const, (b)NGWSGG-Const, and (c)NGWSGG-Mie.
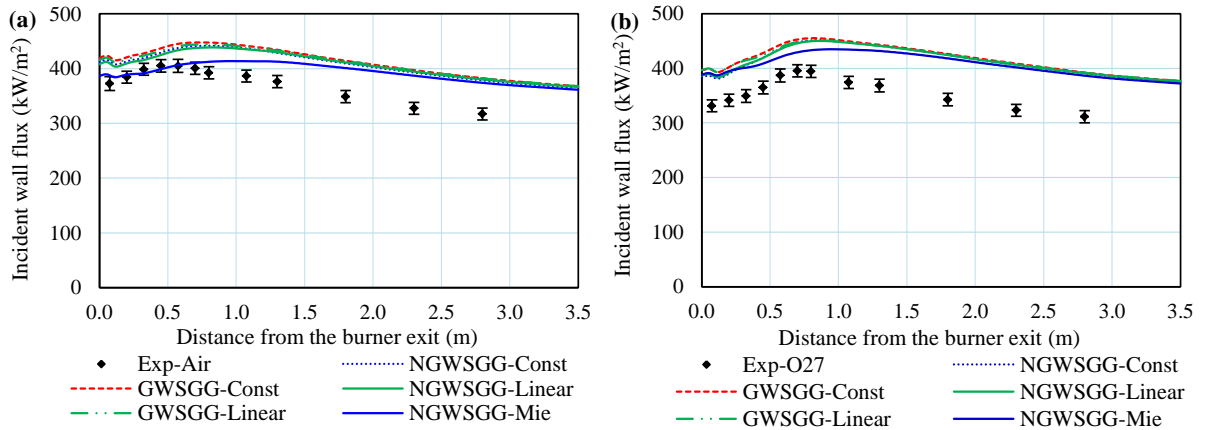
Fig. 6: CFD results for surface incident radiative heat fluxs for (a) air-fired condition, and (b) oxy-27 condition compared to experimental data from [23].
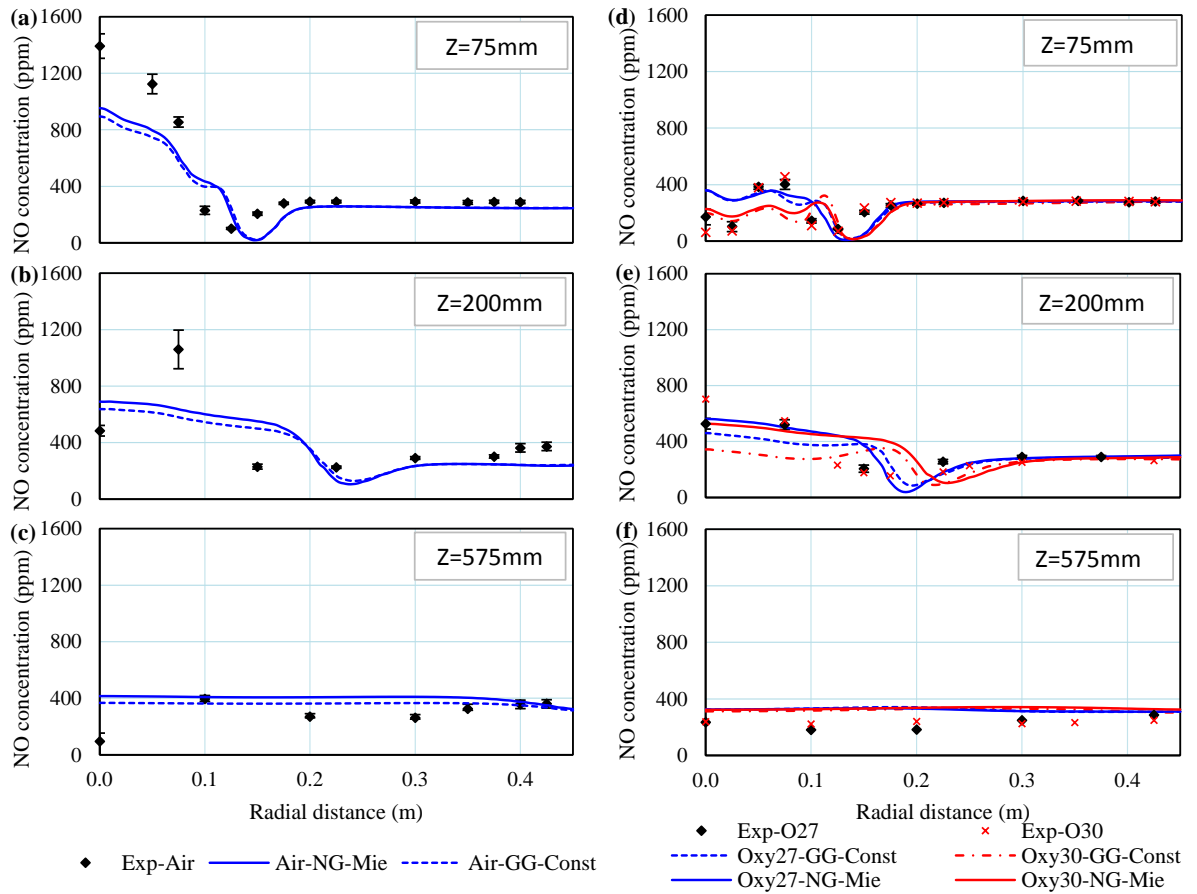
Fig. 7: Radial NO distribution at 75 mm, 200 mm and 575 mm from the burner exit for (a-c) air-fired condition and (d-f) oxy-fired conditions.
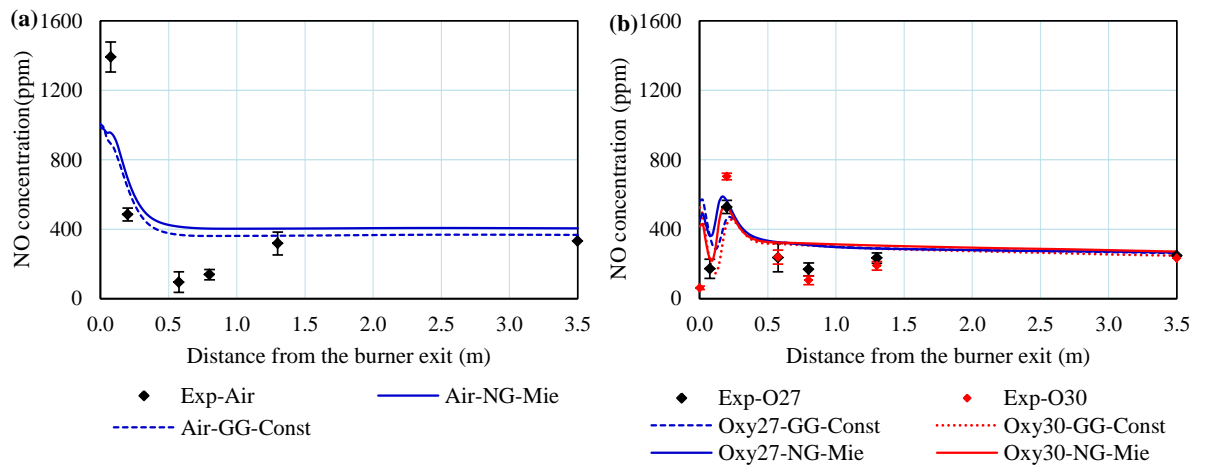
Fig. 8: Axial NO distributions were measured at the centreline of the furnace for (a) air-fired condition, and (b) oxy-fired conditions.
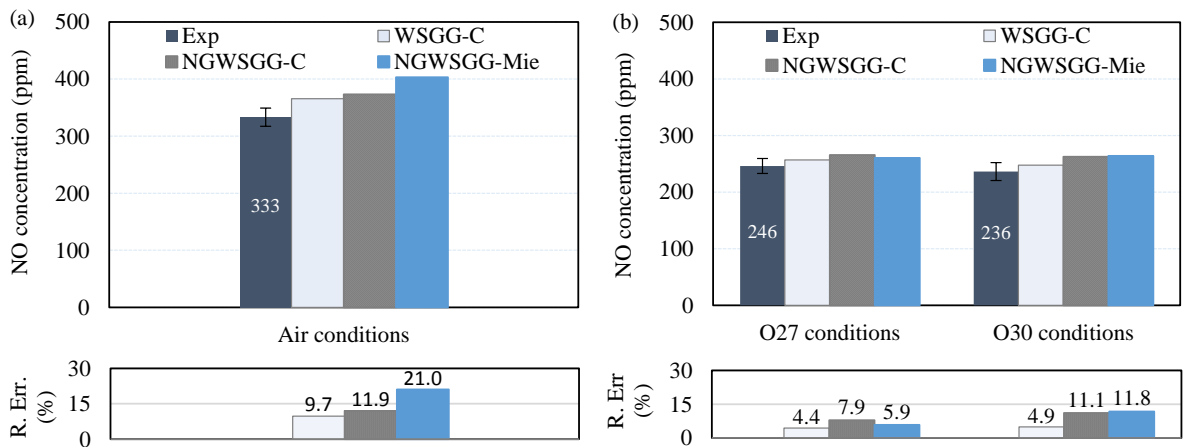

Fig. 9: The average NO concentration at the exit section of the furnace from experimental measurement and CFD calculation for (a) air-fired condition, and (b) oxy-fired conditions.
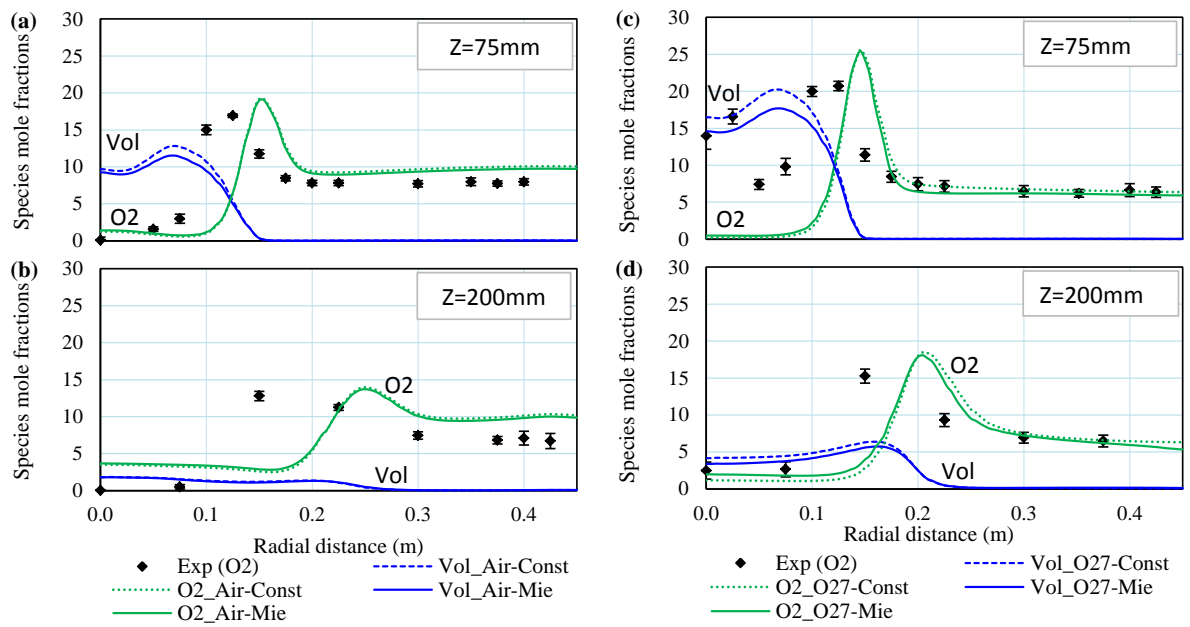
Fig. 10: Results for radial oxy and volatile distribution at 75 mm and 200 mm from the burner exit for (a, b) air-fired condition and (c, d) oxy-27 condition compared to experimental data from [23].